energies

MDPI

Article

AC Magnetic Loss Reduction of SLM Processed Fe-Si for Additive Manufacturing of Electrical Machines

Hans Tiismus [1,*], Ants Kallaste [1], Anouar Belahcen [2], Marek Tarraste [3], Toomas Vaimann [1], Anton Rassõlkin [1], Bilal Asad [1] and Payam Shams Ghahfarokhi [1]

[1] Institute of Electrical Power Engineering and Mechatronics, Tallinn University of Technology, 19086 Tallinn, Estonia; ants.kallaste@taltech.ee (A.K.); toomas.vaimann@taltech.ee (T.V.); anton.rassolkin@taltech.ee (A.R.); bilal.asad@taltech.ee (B.A.); payam.shams@taltech.ee (P.S.G.)
[2] Department of Electrical Engineering and Automation, Aalto University, 02150 Espoo, Finland; Anouar.Belahcen@aalto.fi
[3] Department of Mechanical and Industrial Engineering, Tallinn University of Technology, 19086 Tallinn, Estonia; marek.tarraste@taltech.ee
* Correspondence: hans.tiismus@taltech.ee

Abstract: Additively manufactured soft magnetic Fe-3.7%w.t.Si toroidal samples with solid and novel partitioned cross-sectional geometries are characterized through magnetic measurements. This study focuses on the effect of air gaps and annealing temperature on AC core losses at the 50 Hz frequency. In addition, DC electromagnetic material properties are presented, showing comparable results to conventional and other 3D-printed, high-grade, soft magnetic materials. The magnetization of 1.5 T was achieved at 1800 A/m, exhibiting a maximum relative permeability of 28,900 and hysteresis losses of 0.61 (1 T) and 1.7 (1.5 T) W/kg. A clear trend of total core loss reduction at 50 Hz was observed in relation to the segregation of the specimen cross-sectional topology. The lowest 50 Hz total core losses were measured for the toroidal specimen with four internal air gaps annealed at 1200 °C, exhibiting a total core loss of 1.2 (1 T) and 5.5 (1.5 T) W/kg. This is equal to an 860% total core loss reduction at 1 T and a 510% loss reduction at 1.5 T magnetization compared to solid bulk-printed material. Based on the findings, the advantages and disadvantages of printed air-gapped material internal structures are discussed in detail.

Keywords: electric machines; additive manufacturing; soft magnetic materials; selective laser melting; iron losses; magnetic properties

Citation: Tiismus, H.; Kallaste, A.; Belahcen, A.; Tarraste, M.; Vaimann, T.; Rassõlkin, A.; Asad, B.; Shams Ghahfarokhi, P. AC Magnetic Loss Reduction of SLM Processed Fe-Si for Additive Manufacturing of Electrical Machines. *Energies* **2021**, *14*, 1241. https://doi.org/10.3390/en14051241

Academic Editors: Carlos Platero and Andrea Mariscotti

Received: 27 December 2020
Accepted: 20 February 2021
Published: 24 February 2021

1. Introduction

Metal additive manufacturing (AM) technology has matured, with its capabilities currently outperforming conventional manufacturing methods in several applications. In particular, selective laser melting (SLM), a powder bed fusion (PBF)-based technology, has found widescale utilization for the production of high-performance metallic parts, such as more efficient and long-lasting inductor coils [1], stronger, cheaper and lighter aircraft fuel nozzles [2] and high-performance heat exchangers [3]. The main advantage of SLM is the capacity for the cost-effective production of complex metal part topologies with high spatial accuracy. This enables the implementation of next-generation, topology-optimized components (with reduced weight, cooling channels, reduced inertia, increased heat exchange, etc.) with minimal preparation steps (new molds, jigs, tools, staff training) and manual work required [4].

In addition to the printing structural, thermal and electrical components, the additive manufacturing of magnetic materials has gained significant interest over recent years, focusing mainly on realizing 3D-printed, topology-optimized electromechanical components and electrical machines. Since their inception, the design of electrical machines (EMs) has remained largely unchanged. Most of the machines exhibit a planar design, which can

be characterized and simulated accurately in 2D. It can be proposed that with the ready availability of computational power and the free-form printing capabilities of SLM systems, next-generation electrical machine designs could be modeled and constructed (supported by the rapid prototyping capabilities of AM) by the research community. Presently, however, due to the limited metal multimaterial printing capabilities of SLM systems (with dual selective metal deposition printers emerging just recently [5]), research groups have yet to print an EM with improved performance or efficiency over conventional EMs. The printing of three material types in parallel is required to complete an EM: a diamagnetic material with high electrical conductivity (electromagnetic coils), a ferromagnetic material with low electrical conductivity (magnetic core) and a dielectric material (insulation for both the core and coils). The state-of-the-art additive manufacturing of EMs involves the printing of conductive and soft magnetic materials with air gaps partitioning the material structure to separate individual turns in coils and reduce the induced eddy currents in soft magnetic cores [6]. After printing, the components are postprocessed before assembling the full machine: printing supports cut, cleaning and polishing necessary surfaces and typically annealing the furnace for material homogenization and grain recrystallization. All the necessary individual components for assembling an EM (except the bearings) have successfully been printed with SLM; e.g., solid soft magnetic rotor [7] and stator designs [8], gapped electromagnetic coils [9,10], hairpin windings for traction motors [11] and partitioned (various geometries) soft magnetic cores [12]. Even some upgrades for the existing designs have been presented, such as printed heat guides for supplementary heat evacuation paths for machine areas particularly susceptible to high power loss [13,14].

Presently, compared to the SLM printing of aluminum or copper alloy electrically conductive components, the additive manufacturing of soft magnetic guides for electrical machine applications is still relatively undeveloped and is not presently utilized for commercial applications. This is mostly due to the difficulties in limiting the classical eddy current losses in the printed material. The lack of insulating materials in core construction results in unsuppressed induced classical eddy currents, which are proportional to the strength and rate of change of the magnetic field in the material, the material conductivity and the area of the current loop [15]. These increased classical eddy current losses would not be significant in 3D-printed applications coupled through a quasistatic magnetic field, such as magnetic clutches, gears or rotors of synchronous machines. In 3D-printed bulk (unlaminated) EM stator constructions or induction machine rotors, however, due to the rotating magnetic fields, undesirable thermal heating is generated, which would reduce the additively manufactured component and overall machine efficiency. Several strategies have been suggested to address this, such as improving the chemical composition of the printed material (increasing material resistivity), the printing of intermetallic layers between soft magnetic layers (as polymers and ceramics cannot be processed through SLM) or through the printing of novel material internal structures (air gaps for partitioning the geometry) [16]. The printing of intermetallic layers in magnetic guides with current SLM systems is challenging (powder mixing, controlling the powder deposition); however, it can potentially evolve into the preferred method for classical eddy current losses reduction with the advent of multimaterial SLM printers [5].

In this paper, we utilize the printing of finite internal material structures, which has been shown to effectively reduce the classical eddy current generation considerably [12,16,17] as the segregation of the core volume and the reduction of effective induced current loops can be achieved. It is important to note, however, that introducing air gaps to the material would also reduce its filling factor, lowering the total flux conducted per volume of the material. This could result in a reduced machine air gap magnetic flux density (reduced machine torque), an increased excitation current in the windings to achieve the same magnetic saturation of the material (increased copper losses) or an increased volume of the machine to compensate for the reduced filling factor (reduced power density). Despite the increased volume, however, the specific power (W/kg) of the printed machine would remain largely

unchanged, and the air gaps in the material would increase its effective surface area for heat exchange, suggesting the method's superiority for specific machine designs.

This paper investigates the effect of printed air gaps on the total core losses of additively manufactured 3.7% silicon steel toroidal samples. Two sets of three toroidal designs with unique cross-sections are prepared through SLM and characterized for magnetic loss behavior. Both sets, along with bars for material conductivity measurements and cuboids for material microstructure investigation, undergo thermal annealing, the first up to 800 °C and the second up to 1200 °C. The material characteristics measured are applicable for the further optimization of additively manufactured soft magnetic flux guides for the end goal of developing novel electrical machine designs.

2. Powder, Printer and Sample Characterization

2.1. Powder Characterization

Prealloyed, gas-atomized, commercially available Fe-Si powder provided by Sandvik group was used to fabricate the specimens by SLM. The chemical composition analysis was conducted with both energy-dispersive X-ray spectroscopy (EDX) and atomic emission spectroscopy (AES) measurements, and the results are summarized in Table 1.

Table 1. Summary of the powder chemical composition.

Elements	Fe	Si	Mn	Cr	Ni	C
Wt %	Balance	3.7	0.2	0.16	0.020	0.01

The powder consisted of roughly spherical particles in the size range of 29–58 µm, with a median diameter of 38 µm (d50), as shown in Figure 1. The powder size distribution was determined with a laser-scattering particle size distribution analyzer in a water-dispersive environment, and the shape of the powder particles was confirmed with scanning electron microscopy (SEM).

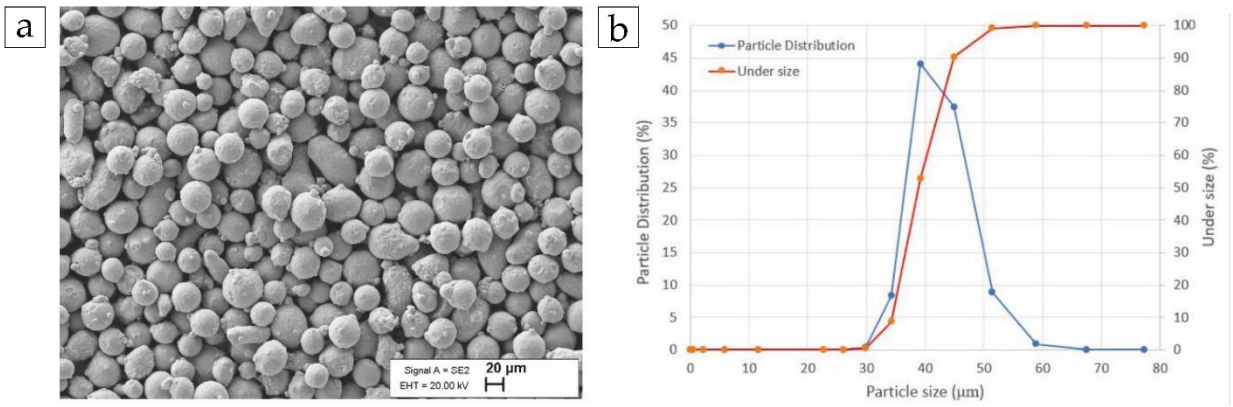

Figure 1. (**a**) SEM magnification of the investigated powder; (**b**) powder particle size distribution and percentage of particles below a specific particle size.

2.2. Printing System and Parameters

All samples were prepared on an SLM Solutions GmbH Realizer SLM-280 machine, suitable for medium- to high-volume metal additive manufacturing part and prototype production. The printing system provides a 280 × 280 × 350 maximum build envelope and dual-scanning 1070 nm yttrium scanning lasers (2 × 400 W). For scientific purposes, a custom, smaller build platform (D100 mm) and recoater were designed and produced for reducing the raw powder quantity needed for printing and streamlining the powder exchange between research projects utilizing different powders. The custom add-ons to the printer are shown in Figure 2. All the samples were printed with a laser remelting

strategy, with a stripe (10 mm wide) scan pattern utilizing a 30° rotation between layers. The remelting strategy was utilized in this study as the incremental energy input reduces particle ejection from the melt pool (sputtering), reducing the irregularities in the solidified part and increasing the spatial accuracy of finite structures (reduced surface roughness [18]) such as printed laminations. Furthermore, it has been shown that grain structure refinement [19] and the development of preferred grain orientation [20] are achievable with annealed laser remelted samples. A summary of the printing parameters is presented in Table 2. The parameters are suitable for printing Fe-Si parts with approximately 99% relative density. All of the printing was conducted in a nitrogen inert gas environment, considering its relatively low cost compared to argon gas. Preheating was not utilized as the custom reduced platform was not equipped for it (the platform temperature remained at approximately 60 °C throughout the printing processes).

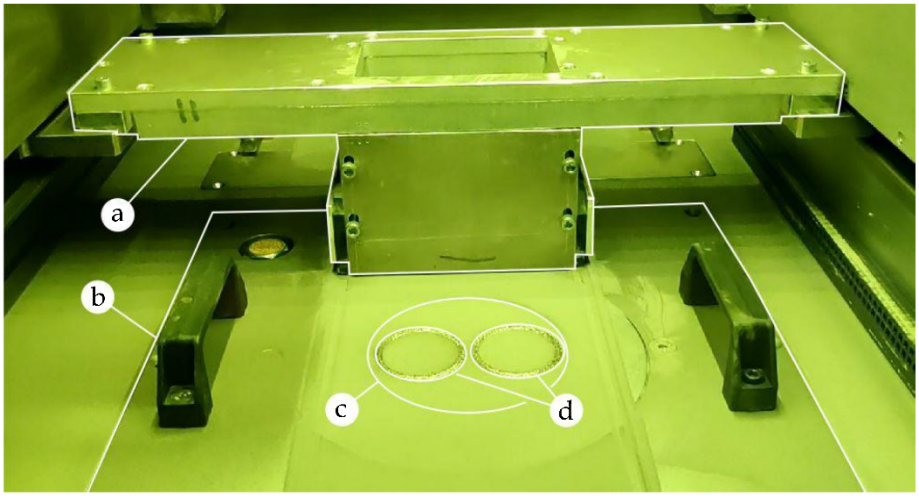

Figure 2. SLM 280 build chamber with custom components: (**a**) recoater; (**b**) build chamber base; (**c**) custom build platform; (**d**) printing of toroidal specimens.

Table 2. Summary of the printing parameters.

Parameter	Initial
Layer thickness	50 µm
Hatch distance	120 µm
Laser power	250 W (primary)/100 W (secondary)
Scanning velocity	0.5 m/s (primary)/0.5 m/s (secondary)
Scan strategy	Stripes
Laser spot size	~120 µm
Preheating	NA
Environment	Nitrogen
Oxygen content	~0.1%

2.3. Samples

In this study, the effect of both the introduction of air gaps to the material and the annealing temperature on the magnetic properties were investigated. Three toroidal designs were printed with the same toroid diameter (outer diameter of 45 mm), thickness (3 mm) and height (6 mm), with different cross-sections: solid, a single air gap in the middle of the toroid and four air gaps dividing the toroid thickness equally. The individual laminations were connected through thin lattice-like bridges. The design with four air gaps also included two chokes for each lamination for additional current path resistance. The width of the air gaps was chosen as the minimum gap width, which enables the removal of unfused powder from between the laminations (to avoid unmelted powder sintering between the laminations during annealing). The diameter of the toroids was

chosen based on the build platform diameter to print two toroids simultaneously while fulfilling the standardized [21] criteria for the ratio of the inner and outer diameters of the toroid. The different designs were chosen to study the effects of both the printed air gaps and consequently the reduced filling factor on the core loss behavior of the printed material. In addition to the toroids, six bar samples of 3 × 3 × 45 mm were printed (only in horizontal alignment in relation to the build platform) to measure the electrical resistivity in as-built and annealed conditions (both 800 and 1200 °C). The summary of the printed sample geometries is presented in Table 3. For each toroidal design, one toroid was annealed at 800° and the other at 1200° for the investigation of its effect on the material core losses (higher conductivity -> higher classical eddy current, lower internal stress -> reduced hysteresis loss, higher grain size -> reduced hysteresis loss, increased anomalous eddy current loss [22]). In all instances, annealing was performed in a vacuum environment (~0.1 mbar), with a heating rate of 300 K/h, kept at the target temperature for 1 h and then slowly furnace-cooled to room temperature.

Table 3. Summary of the printed samples.

Type	Quantity	Dimensions
Toroid solid	2	Cross-section of 3 × 6 mm, outer diameter of 45 mm, no air gaps
Toroid single gap	2	Cross-section of 3 × 6 mm, outer diameter of 45 mm, one air gap
Toroid multiple gaps	2	Cross-section of 3 × 6 mm, outer diameter of 45 mm, four air gaps
Bars	6	Cuboids of 3 × 3 × 45 mm
Cubes	3	Cuboids of 3 × 6 × 6 mm with no, one and four air gaps

For determining the filling factor and the porosity of the printed material, cuboidal 3 × 6 × 6 mm samples with no, one and four air gaps were printed. The structure of the printed samples was evaluated with standard metallographic practices with polishing and optical microscopy. The porosity and filling factor were determined from the processing of the thresholded images. The average sample absolute density was calculated from the volume and the weight of the toroidal samples (the Archimedes scale method is unsuitable due to captured air bubbles between the laminations). Cross-sectional images of the printed air gaps are presented in Figure 3, as well as a summary of the material density analysis in Table 4.

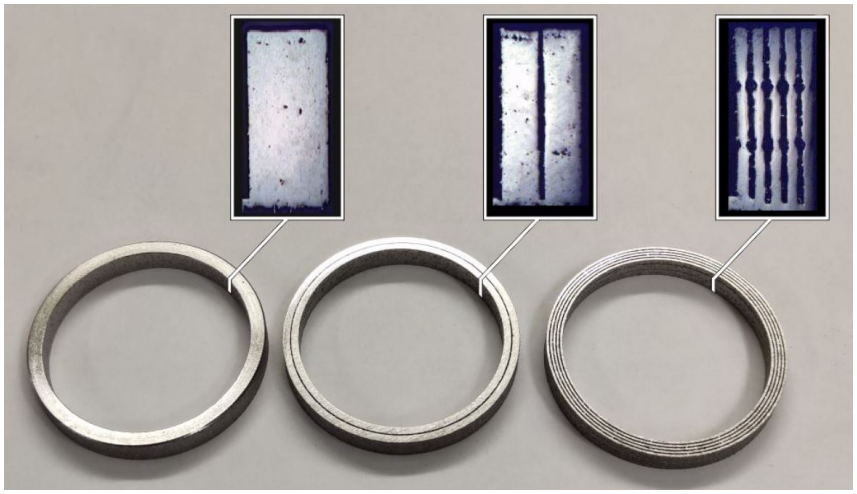

Figure 3. Variations of printed ring samples for magnetic characterization: solid (**left**); single gap (**middle**); multiple gaps (**right**).

Table 4. Summary of the printed toroid density.

Type	Absolute Density (kg/m^3)	Relative Density (%)	Filling Factor
Toroid solid	7750	99.2	1
Toroid single gap	7140	98.6	0.92
Toroid multiple gaps	4620	99.6	0.59

3. Methods for Material Electromagnetic Characterization

The ring method was employed for the measurement of material magnetic properties. The measurements were conducted at the frequencies of 25 MHz (for quasistatic properties) and 50 Hz (for the investigation of AC losses). The measurements were completed in accordance with the European standards EN 60404-6 [21] and EN 60404-4 [23]. A schematic of the magnetic measurements setup is shown in Figure 4a, as well as a measured sample in Figure 4b. A Dewetron DEWE2-M data acquisition system at a 10 kHz sampling frequency was used for saving the induced voltage of the experiments, and a sinusoidal excitation current was used. Signal Amplifier Omicron CMS 356 was used for amplifying the generated signal from the waveform generator and maintaining its sinusoidal waveform throughout the experiment. Experiments were conducted at the ambient temperature of ~20 °C, without a significant increase in the sample temperature during the measurements. From the experimental data, the magnetic field strength H was calculated by (1) and the average flux density B by (2):

$$H = \frac{N_1 i}{l_t} \tag{1}$$

$$B = \frac{1}{N_2 \cdot S \cdot F} \int_t e(t) dt \tag{2}$$

where N_1 is the number of turns of the primary coil, N_2 is the number of turns of the secondary coil, i is the instantaneous current value, e is the instantaneous induced electromotive force, l_t is the toroid average length, S is the toroid cross-sectional area and F is the material filling factor. The specific core losses (P_s) were then found from the integration of the curve areas, considering both the average density of the material (ρ) and period (T) of each hysteresis cycle, as expressed in (3).

$$P_s = \frac{1}{T\,\rho} \left(\int_0^T H_1 dB_1 - \int_0^T H_2 dB_2 \right) \tag{3}$$

The electrical resistivity of the printed material was evaluated with the four-probe Kelvin sensing method [24]. The test schematic of the electrical measurements setup is shown in Figure 4c. Test jig was built from 3D-printed plastic parts and a set of vices to clamp the test specimens between the Kelvin probes, shown in Figure 4d. Both ends of the bars were polished, and aluminum-based conductive paste was added between the probes to minimize the contact resistance. The resistance of the samples was calculated from the slope of the V–I measurements and resistivity (ρ) from (4), where R is the sample resistance, A is the cross-sectional area and l the length of the test specimens.

$$\rho = R\,\frac{A}{l} \tag{4}$$

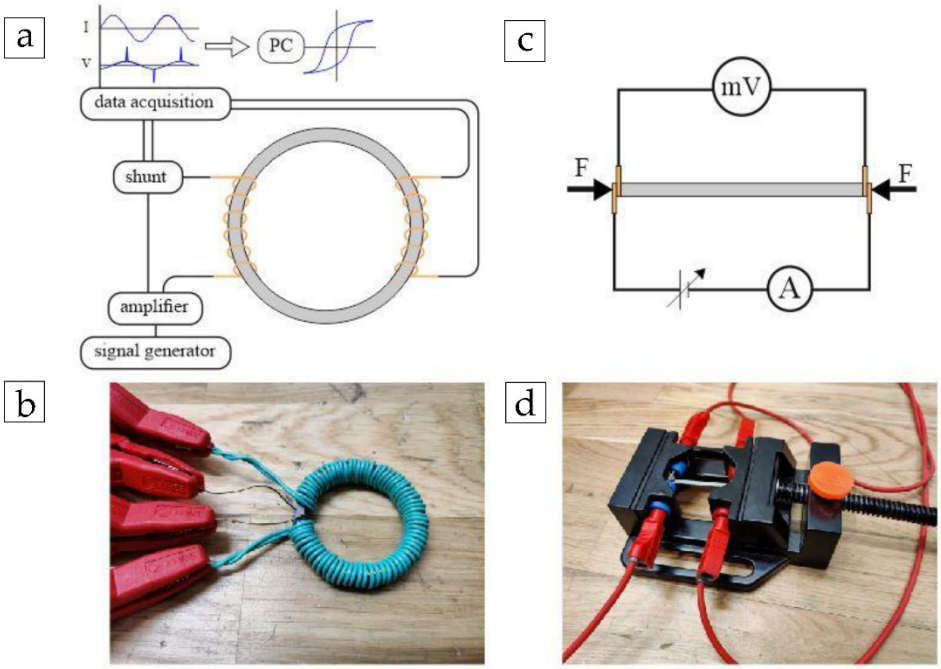

Figure 4. (**a**) Schematic of the magnetic measurements; (**b**) wound toroidal sample; (**c**) schematic of the resistivity measurements; (**d**) measurement of the rod in the test jig.

4. Results of the Electromagnetic Measurements

4.1. DC Material Properties

The measured DC hysteresis loops of three solid toroidal specimens with varying heat treatments at the magnetization of 1.5 T are presented in Figure 5, as well as the corresponding relative permeabilities. On average, 1.5 T magnetization was achieved at 1800 A/m, with the unannealed specimen requiring the highest magnetic field strength of 2500 A/m. Both coercivity and permeability exhibited a monotonous trend in relation to annealing temperature: coercivity increased from 41 A/m (1200 °C) to 132 A/m (800 °C) and 205 A/m (unannealed) and maximum relative permeability decreased from 28,900 (1200 °C) to 7460 (800 °C) and 3220 (unannealed).

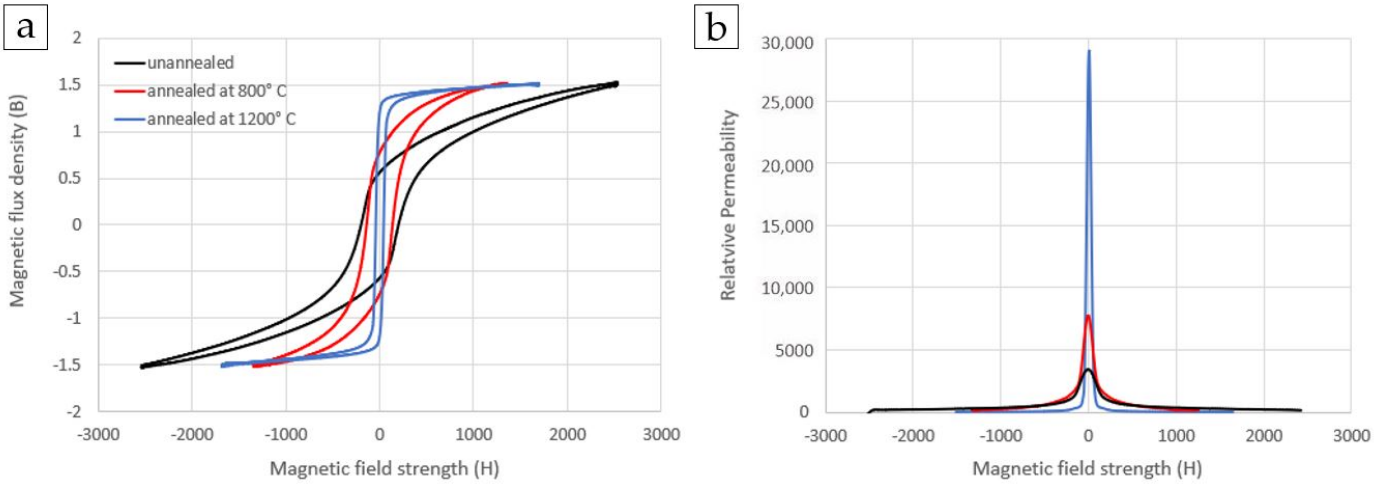

Figure 5. (**a**) DC hysteresis curves of the printed solid toroidal specimens with varying heat treatments. (**b**) Relative permeability corresponding to the DC hysteresis curves.

Hysteresis losses exhibited a monotonous decrease in relation to both an increased heat treatment temperature and the lower magnetization of the material. The calculated

specific hysteresis losses per cycle are presented in Figure 6. The hysteresis losses at 1.5 T, 50 Hz ($W_{15/50}$) magnetization ranged from 7.0 W/kg (unannealed) to 5.3 W/kg (800 °C) and 1.7 W/kg (1200 °C). At 1 T, 50 Hz ($W_{10/50}$) magnetization, the losses were substantially lower, ranging from 3.9 W/kg (unannealed) to 2.6 W/kg (800 °C) and 0.58 W/kg (1200 °C). The hysteresis loss behavior in gapped toroids remained largely unchanged compared to the solid toroid. The resistivity of the material showed a monotonous decrease with an increased heat treatment temperature, ranging from 71.4 μΩ·cm (unannealed) to 59.2 μΩ·cm (800 °C) and 56.9 μΩ·cm (1200 °C). A summarization of the characterized material DC electromagnetic properties is presented in Table 5.

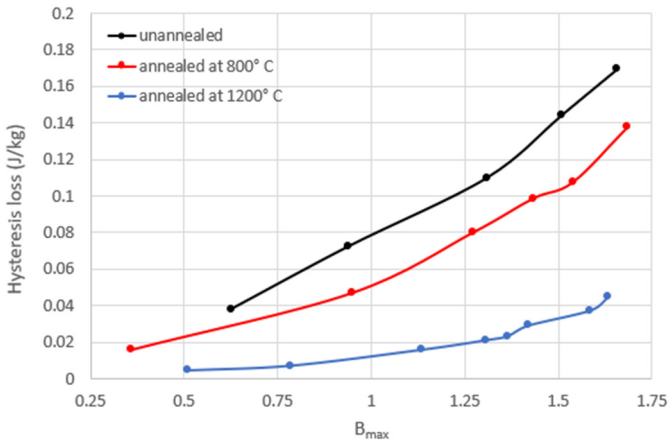

Figure 6. Hysteresis losses of the printed solid toroidal specimens with varying heat treatments.

Table 5. Summary of the DC electromagnetic properties of the printed specimens.

Type	Unit	As-Built	Annealed 800 °C	Annealed 1200 °C
Maximum relative permeability	-	3220	7460	28,900
Hysteresis loss at 1.5 T, 50 Hz	W/kg	7.0	5.3	1.7
Hysteresis loss at 1.0 T, 50 Hz	W/kg	3.9	2.6	0.61
Coercivity at 1.5 T	A/m	205	132	41
Electrical Resistivity	μΩ·cm	71.4	59.2	56.9

4.2. AC Core Losses

All the AC core loss measurements were conducted at a 50 Hz supply frequency in the magnetization range of 0.4–1.6 T. For all the calculations, the effective cross-sectional area of the metal laminations was used (air gap area subtracted from the full cross-sectional area), and the fill factor for each cross-section is presented in Table 4. AC core losses were characterized in two sets (annealed at 800 and 1200 °C) of three toroids (fully-dense, a single air gap, four air gaps). Both sets show a clear trend of core loss reduction in relation to the segregation of the specimen cross-sectional topology. The studied hysteresis curves are presented in Figure 7, illustrating the shearing and area growth of the loops due to induced eddy current losses. All the measured AC losses are presented in Figure 8. In all cases, the samples annealed at 1200 °C exhibited lower total core losses than the samples annealed at 800 °C. The lowest AC losses in this study were measured for the toroid with four printed air gaps, exhibiting losses of 1.2 W/kg (1 T) and 5.5 W/kg (1.5 T). The highest AC losses were measured for the solid sample annealed at 1200 °C, exhibiting losses of 15.3 W/kg (1 T) and 30.5 W/kg (1.5 T). A summary of the AC measurements is presented in Table 6.

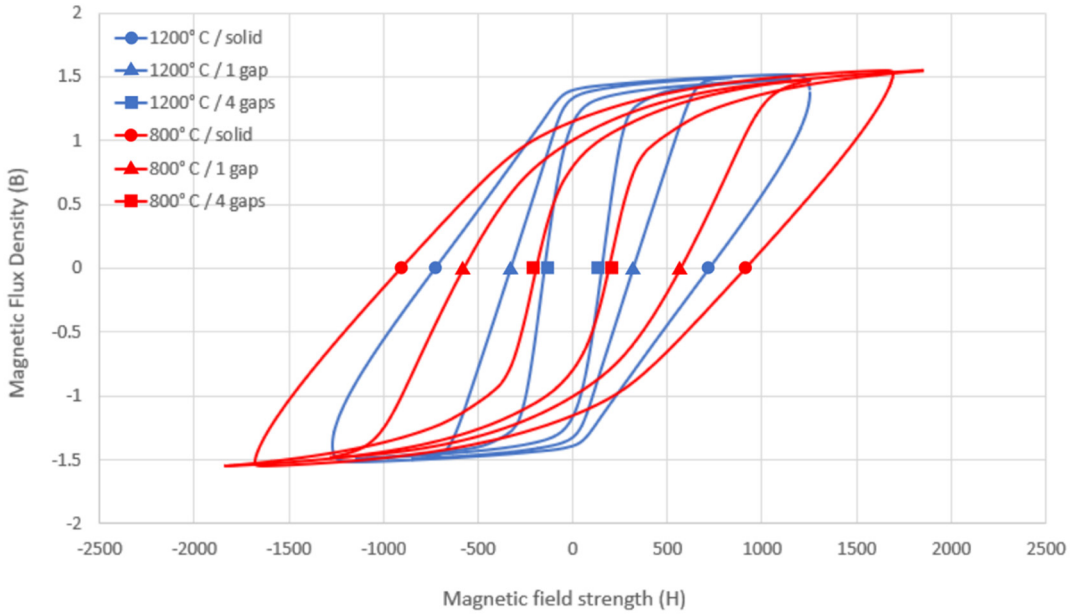

Figure 7. AC hysteresis curves measured at 50 Hz and 1.5 T magnetization with varying heat treatments and cross-sectional topologies.

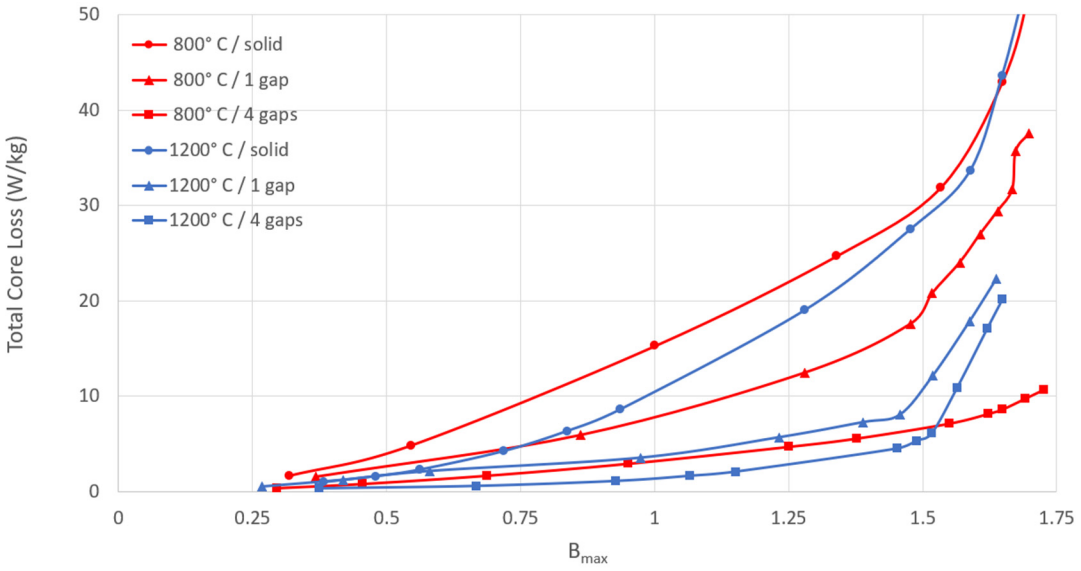

Figure 8. Hysteresis losses of the printed toroidal specimens with varying heat treatments and cross-sectional topologies.

Table 6. Summary of AC magnetic properties of the printed specimens.

Type	Annealed 800 °C (W/kg)	Annealed 1200 °C (W/kg)
Solid/total loss at 1 T, 50 Hz	15.3	10.4
Single gap/total loss at 1 T, 50 Hz	7.5	3.6
Four gaps/total loss at 1 T, 50 Hz	3.3	1.2
Solid/total loss at 1.5 T, 50 Hz	30.5	28.3
Single gap/total loss at 1.5 T, 50 Hz	18.3	11.7
Four gaps/total loss at 1.5 T, 50 Hz	6.6	5.5

A sharp increase in loss behavior was observed when magnetizing the samples beyond saturation. The inflation of core loss was more intense for all of the samples annealed at 1200 °C and least prominent for the sample with four air gaps annealed at 800 °C

5. Discussion

The DC magnetic properties of the printed material characterized in this study are compared with conventional nonoriented electrical steels and other additively manufactured soft magnetic materials. Hysteresis losses of 0.61 ($W_{10/50}$) and 1.7 ($W_{15/50}$) W/kg were obtained in this study. In the case of nonoriented (NO) Fe-3%w.t.Si sheets, the hysteresis loss component is typically in the range of 1.8–2.1 W/kg ($W_{15/50}$) [25]. For NO 6.5% silicon steel sheets, the hysteresis losses have been shown to range between 0.5 and 0.7 W/kg ($W_{10/50}$) [15]. For low-carbon (0.04–0.06%) steels, the hysteresis losses can even reach up to 5.5–10 W/kg ($W_{15/50}$) [15]. Despite grain-oriented (GO) steels having superior magnetic behavior to the printed and conventional NO materials (in the range of 0.34 W/kg ($W_{17/50}$), magnetized in the grain direction [25], these materials are not the best suited for electrical machine applications due to multidirectional magnetization required. GO steels show a similar loss behavior of 1.7 W/kg ($W_{15/50}$) when magnetized perpendicularly to the grain direction.

The total core losses for NO silicon steel laminations (typically 0.35–0.5mm thick) range from 2.2 to 2.5 W/kg ($W_{15/50}$) for top grades, 4–6 W/kg ($W_{15/50}$) for medium grades and 7–9 W/kg ($W_{15/50}$) for low-grade material [15]. For grain-oriented steel laminations, total core losses (when magnetized in the grain direction) can be as low as 0.6–1 W/kg ($W_{15/50}$) [15]. For SLM-printed silicon steel, only total core losses have been investigated, with the exception of Goll et al. [16], showing hysteresis of 0.7 W/kg ($W_{10/50}$) for the 6.5% silicon content toroidal samples. In the same study, total core losses of 6.5 W/kg ($W_{10/50}$) were observed (a 5 × 5 mm toroidal sample with a 35 mm outer diameter). Garibaldi et al. [26] measured the total core losses of 4 W/kg ($W_{10/50}$) in 6.9% silicon steel toroidal samples (a 4.55 × 2 mm toroidal sample with a 28 mm cross-section). Plotkowski et al. [17] observed the lowest total core losses of 1.34 W/kg ($W_{10/50}$) for samples with segregated ("Hilbert" pattern with a 56% fill factor) core cross-sections (four bars exhibiting a 6.35 mm^2 cross-section with a length of 63.5 mm). The same authors in [12] showed approximately 5 W/kg (3% silicon steel) and 3.3 W/kg (6% silicon steel) total core losses ($W_{15/60}$) for an additively manufactured full E-type transformer core with the same "Hilbert" pattern flux guide cross-section. These measured power losses are comparable to the total core losses obtained in the current study: 1.2 W/kg ($W_{10/50}$) and 5.5 W/kg ($W_{15/50}$) for the toroidal specimen with four air gaps (a 35 × 6 mm toroidal sample exhibiting a 45 mm outer diameter and a 0.59 fill factor).

Electrical resistivity measured in this study correlated with the literature. Annealed 3.7% silicon samples exhibited a resistivity of 56.9 μΩ·cm. The observed 20% reduction in postannealed material resistivity can be caused by the homogenization effect of the annealing treatment to the material internal structure, as observed in [27,28]. Typical resistivity values for 3% and 6% silicon steels are 47 [15] and 82 [29] μΩ·cm, respectively, showing a nearly linear relationship between resistivity and silicon content over the range of 3–8 wt% [28], which corresponds to 54 μΩ·cm for 3.7% silicon content steel. Although the influence of the build orientation [24] on the material resistivity was not investigated in this study for the Fe-Si alloy, homogeneous material resistivity, invariant from the build orientation, has mostly been shown for Cu [27] and $AlSi_{10}Mg$ [28] alloys after furnace annealing.

A gapped material structure and the reduction of its filling factor provide both advantages and disadvantages for the realization of electromechanical components. On the one hand, the volumetric sizes of the components would need to increase to sustain the same total flux as printed solid or conventional laminated designs. With a filling factor of 0.59 (design in Table 4), the printed component must be printed 1.7× larger than its solid counterpart. Even so, the increased size would provide an additional cooling capacity to the component as it exhibits a larger effective surface area for heat exchange. In this study, the total surface area of the investigated toroids increased up to 370% with the introduction of the air gaps to the material. The increased surface area of the magnetic cores can potentially be realized for different fluid-based cooling methods (oil immersion, forced convection,

etc. [30]) for the printed components, which benefit from the low cost-to-complexity ratio of SLM.

Currently, the main challenges related to the large air gap widths in the material are the spatial accuracy of the printing systems and postprinting powder removal. Narrow air gaps can be responsible for short circuits between laminations due to irregularities in the air gap, related to particle ejection and sputtering during printing. Unremovable powder between the laminations can be responsible for increased eddy current losses in the component due to powder sintering between the laminations during annealing. Furthermore, unremoved powder or narrow air gaps would reduce the cooling capacity of the air-gapped design. With multimaterial printing, the filling factor can potentially be significantly increased as more control can be obtained for insulating layer formation. It is likely that with the advent of multimaterial metal printers [5,31], the most effective cores would exhibit hybrid designs, incorporating both air-gapped designs and intermetallic insulating layers for maximum efficiency: dense multimaterial structures for machine areas, where the flux density is near saturation, and bioinspired [32] gapped structures, where the flux density is lower for the optimized thermal cooling of the core. In these types of cores, traditional laminated designs can evolve into more complex shapes for additional loss reduction (such as the "Hilbert" material topology in [26]).

6. Conclusions

The material characterized in this study is well-applicable for developing optimized additively manufactured soft magnetic components and novel electrical machine designs. Excellent DC magnetic properties of the printed material were obtained, and the magnetization of 1.5 T was achieved at 1800 A/m, exhibiting a maximum relative permeability of 28,900 and hysteresis losses of 0.61 (1 T) and 1.7 (1.5 T) W/kg. A reduction in AC losses of the printed magnetic core was achieved in this study through the introduction of air gaps into the topology, effectively limiting the core eddy current losses by reducing the effective area of the induced current loops. A clear trend of core loss reduction in relation to the increased segregation of the specimen cross-sectional topology was observed for all samples. Total core and hysteresis losses were lower for all specimens annealed at the higher temperature of 1200 °C. In total, 860% total core loss reduction was obtained at 1 T and a 510% loss reduction at 1.5 T magnetization. Minimal losses in this study were obtained from the toroidal specimen annealed at 1200 °C and prepared with four internal air gaps. The losses ranged from 5.5 ($W_{15/50}$) to 1.2 ($W_{10/50}$) W/kg. A reduction of 20% in material resistivity was observed as the effect of sample annealing. From 71.4 (unannealed) to 56.9 μΩ·cm (1200 °C), however, only a modest difference of 4% in resistivity was measured for the specimens processed with a moderate and high annealing temperature. Despite the increased volume of the air-gapped printed components to deliver the same total flux, improved thermal capabilities of the design are proposed as higher effective surface area for the same component weight can be achieved.

The designs presented in the work are the first steps in the field and are promising; however, further material optimization can be achieved. Future work on the project will involve the investigation of more complex printed flux guide topologies to achieve further loss reduction, with a higher material fill factor. Furthermore, despite showing a clear trend of loss behavior in this paper, future research demands the investigation of material property variations between individual samples fabricated with identical parameters.

Author Contributions: Conceptualization: A.K. and H.T.; methodology: A.R.; validation, A.K.; investigation, H.T. and M.T.; resources, P.S.G. and B.A.; writing—original draft preparation, H.T.; writing—review and editing, H.T., A.K. and A.B.; supervision, A.K., A.B. and A.R.; project administration, T.V.; funding acquisition, A.K. All authors have read and agreed to the published version of the manuscript.

Funding: This research work has been supported by the Estonian Ministry of Education and Research (Projects PSG-137 and PRG-665).

Institutional Review Board Statement: Not applicable.

Informed Consent Statement: Informed consent was obtained from all subjects involved in the study.

Data Availability Statement: Data is contained within the article.

Acknowledgments: The preparation of micrograph samples and SEM and EDX analyses were supported by the projects IUT-19-28 and TK-141.

Conflicts of Interest: The authors declare no conflict of interest.

References

1. How 3D Printing Is Redefining Inductor Coil Production | GKN Additive. Available online: https://www.gknpm.com/en/our-businesses/gkn-additive/how-3d-printing-is-redefining-inductor-coil-production/ (accessed on 26 November 2020).
2. GE Aviation 3D Prints 30,000th Metal 3D Printed Fuel Nozzle at Auburn, Alabama Plant—3DPrint.com | The Voice of 3D Printing/Additive Manufacturing. Available online: https://3dprint.com/226703/ge-aviation-fuel-nozzle-3d-printed-30000/?fbclid=IwAR38NO-0dAf2BwIkXhVtlC18gAimKnQUSy5KRv-u08InfruK5Zl7Ql1P1HI (accessed on 26 November 2020).
3. Conflux Technology Is Reinventing Heat Exchangers with 3D Printing 3D Printing Media Network—The Pulse of the AM Industry. Available online: https://www.3dprintingmedia.network/conflux-technology-reinventing-heat-exchangers/ (accessed on 26 November 2020).
4. Ngo, T.D.; Kashani, A.; Imbalzano, G.; Nguyen, K.T.; Hui, D. Additive manufacturing (3D printing): A review of materials, methods, applications and challenges. *Compos. Part B: Eng.* **2018**, *143*, 172–196. [CrossRef]
5. Dual Metal LPBF—Aerosint. Available online: https://aerosint.com/dual-metal-lpbf/ (accessed on 27 November 2020).
6. Tiismus, H.; Kallaste, A.; Belahcen, A.; Rassolkin, A.; Vaimann, T. Challenges of Additive Manufacturing of Electrical Machines. In Proceedings of the 2019 IEEE 12th International Symposium on Diagnostics for Electrical Machines, Power Electronics and Drives (SDEMPED), Toulouse, France, 27–30 August 2019; pp. 44–48.
7. Gargalis, L.; Madonna, V.; Giangrande, P.; Rocca, R.; Hardy, M.; Ashcroft, I.; Galea, M.; Hague, R. Additive Manufacturing and Testing of a Soft Magnetic Rotor for a Switched Reluctance Motor. *IEEE Access* **2020**, *8*, 206982–206991. [CrossRef]
8. Rassolkin, A.; Kallaste, A.; Vaimann, T.; Tiismus, H. Control Challenges of 3D Printed Switched Reluctance Motor. In Proceedings of the 2019 26th International Workshop on Electric Drives: Improvement in Efficiency of Electric Drives (IWED), Moscow, Russia, 30 January–2 February 2019; IEEE: New York, NY, USA, 2019; pp. 1–5.
9. Simpson, N.; North, D.J.; Collins, S.M.; Mellor, P.H. Additive Manufacturing of Shaped Profile Windings for Minimal AC Loss in Electrical Machines. *IEEE Trans. Ind. Appl.* **2020**, *56*, 2510–2519. [CrossRef]
10. Ayat, S.; Simpson, N.; Daguse, B.; Rudolph, J.; Lorenz, F.; Drury, D. Design of Shaped-Profile Electrical Machine Windings for Multi-Material Additive Manufacture. In Proceedings of the 2020 International Conference on Electrical Machines (ICEM) 2020, Gothenburg, Sweden, 23–26 August 2020; Volume 1, pp. 1554–1559.
11. More Powerful Electric Motors with 3D Printing: EXIST Research Transfer from TU Freiberg Pushes Additive Manufacturing—Innovations Report. Available online: https://www.innovations-report.com/machine-engineering/more-powerful-electric-motors-with-3d-printing-exist-research-transfer-from-tu-freiberg-pushes-additive-manufacturing/ (accessed on 27 November 2020).
12. Plotkowski, A.; Carver, K.; List, F.; Pries, J.; Li, Z.; Rossy, A.M.; Leonard, D. Design and performance of an additively manufactured high-Si transformer core. *Mater. Des.* **2020**, *194*, 108894. [CrossRef]
13. Wrobel, R.; Hussein, A. Design Considerations of Heat Guides Fabricated Using Additive Manufacturing for Enhanced Heat Transfer in Electrical Machines. In Proceedings of the 2018 IEEE Energy Conversion Congress and Exposition (ECCE) 2018, Portland, OR, USA, 23–27 September 2018; pp. 6506–6513. [CrossRef]
14. Sixel, W.; Liu, M.; Nellis, G.; Sarlioglu, B. Cooling of Windings in Electric Machines via 3-D Printed Heat Exchanger. *IEEE Trans. Ind. Appl.* **2020**, *56*, 4718–4726. [CrossRef]
15. Tumanski, S. *Handbook of Magnetic Measurements*; CRC Press: Boca Raton, FL, USA, 2016.
16. Goll, D.; Schuller, D.; Martinek, G.; Kunert, T.; Schurr, J.; Sinz, C.; Schubert, T.; Bernthaler, T.; Riegel, H.; Schneider, G. Additive manufacturing of soft magnetic materials and components. *Addit. Manuf.* **2019**, *27*, 428–439. [CrossRef]
17. Plotkowski, A.; Pries, J.; List, F.; Nandwana, P.; Stump, B.; Carver, K.; Dehoff, R. Influence of scan pattern and geometry on the microstructure and soft-magnetic performance of additively manufactured Fe-Si. *Addit. Manuf.* **2019**, *29*, 100781. [CrossRef]
18. Yasa, E.; Kruth, J. Application of Laser Re-Melting on Selective Laser Melting Parts. *Adv. Prod. Eng. Manag.* **2011**, *6*, 259–270.
19. Griffiths, S.; Rossell, M.; Croteau, J.; Vo, N.; Dunand, D.; Leinenbach, C. Effect of laser rescanning on the grain microstructure of a selective laser melted Al-Mg-Zr alloy. *Mater. Charact.* **2018**, *143*, 34–42. [CrossRef]
20. Tiismus, H.; Kallaste, A.; Belahcen, A.; Vaimann, T.; Rassõlkin, A.; Lukichev, D. Hysteresis Measurements and Numerical Losses Segregation of Additively Manufactured Silicon Steel for 3D Printing Electrical Machines. *Appl. Sci.* **2020**, *10*, 6515. [CrossRef]
21. European Committee for Electrotechnical Standardization. *European Standard EN 60404-6: Magnetic Materials—Part 6: Methods of Measurement of the Magnetic Properties of Magnetically Soft Metallic and Powder Materials at Frequencies in the Range 20 Hz to 100 kHz by the Use of Ring Specimens*; International Electrotechnical Commission: Geneva, Switzerland, 2004; TC-68; Available online: http://www.evs.ee/et/iec-60404-6-2018 (accessed on 9 December 2020).

22. Tiismus, H.; Kallaste, A.; Rassõlkin, A.; Vaimann, T. Preliminary Analysis of Soft Magnetic Material Properties for Additive Manufacturing of Electrical Machines. *Key Eng. Mater.* **2019**, *799*, 270–275. [CrossRef]
23. European Committee for Electrotechnical Standardization. *European Standard EN 60404-4: Magnetic Materials—Part 4: Methods of Measurement of d.c. Magnetic Properties of Iron and Steel*; International Electrotechnical Commission: Geneva, Switzerland, 2002; TC-68; Available online: https://www.evs.ee/et/evs-en-60404-4-2002 (accessed on 9 December 2020).
24. Tiismus, H.; Kallaste, A.; Vaimann, T.; Rassolkin, A.; Belahcen, A. Electrical Resistivity of Additively Manufactured Silicon Steel for Electrical Machine Fabrication. *SEEM* **2019**, 1–4. [CrossRef]
25. Bertotti, G. General properties of power losses in soft ferromagnetic materials. *IEEE Trans. Magn.* **1988**, *24*, 621–630. [CrossRef]
26. Garibaldi, M.; Ashcroft, I.; Hillier, N.; Harmon, S.; Hague, R. Relationship between laser energy input, microstructures and magnetic properties of selective laser melted Fe-6.9%wt Si soft magnets. *Mater. Charact.* **2018**, *143*, 144–151. [CrossRef]
27. Silbernagel, C.; Gargalis, L.; Ashcroft, I.; Hague, R.; Galea, M.; Dickens, P. Electrical resistivity of pure copper processed by medium-powered laser powder bed fusion additive manufacturing for use in electromagnetic applications. *Addit. Manuf.* **2019**, *29*, 100831. [CrossRef]
28. Silbernagel, C.; Ashcroft, I.; Dickens, P.; Galea, M. Electrical resistivity of additively manufactured AlSi10Mg for use in electric motors. *Addit. Manuf.* **2018**, *21*, 395–403. [CrossRef]
29. Ouyang, G.; Chen, X.; Liang, Y.; Macziewski, C.; Cui, J. Review of Fe-6.5 wt%Si high silicon steel—A promising soft magnetic material for sub-kHz application. *J. Magn. Magn. Mater.* **2019**, *481*, 234–250. [CrossRef]
30. Jafari, D.; Wits, W.W. The utilization of selective laser melting technology on heat transfer devices for thermal energy conversion applications: A review. *Renew. Sustain. Energy Rev.* **2018**, *91*, 420–442. [CrossRef]
31. Aerosint 3D Prints Multi-Metal Parts Using LPBF 3D Printing Media Network—The Pulse of the AM Industry. Available online: https://www.3dprintingmedia.network/aerosint-3d-prints-multi-metal-lpbf/ (accessed on 14 December 2020).
32. Orosz, T.; Rassõlkin, A.; Kallaste, A.; Arsénio, P.; Pánek, D.; Kaska, J.; Karban, P. Robust Design Optimization and Emerging Technologies for Electrical Machines: Challenges and Open Problems. *Appl. Sci.* **2020**, *10*, 6653. [CrossRef]